







Article

In Situ Assembly of Well-Defined MoS₂ Slabs on Shape-Tailored Anatase TiO₂ Nanostructures: Heterojunctions Role in Phenol Photodegradation

Rosangela Santalucia , Paolo Negro , Tiziano Vacca, Francesco Pellegrino , Alessandro Damin , Federico Cesano *  and Domenica Scarano * 

Department of Chemistry and NIS (Nanostructured Interfaces and Surfaces) Interdepartmental Centre, University of Torino & INSTM-UdR Torino, Via P. Giuria 7, 10125 Torino, Italy

* Correspondence: federico.cesano@unito.it (F.C.); domenica.scarano@unito.it (D.S.); Tel.: +39-011-6707548 (F.C.); +39-011-6707834 (D.S.)

Abstract: MoS₂/TiO₂-based nanostructures have attracted extensive attention due to their high performance in many fields, including photocatalysis. In this contribution, MoS₂ nanostructures were prepared via an in situ bottom-up approach at the surface of shape-controlled TiO₂ nanoparticles (TiO₂ nanosheets and bipyramids). Furthermore, a multi-technique approach by combining electron microscopy and spectroscopic methods was employed. More in detail, the morphology/structure and vibrational/optical properties of MoS₂ slabs on TiO₂ anatase bipyramidal nanoparticles, mainly exposing {101} facets, and on TiO₂ anatase nanosheets exposing both {001} and {101} facets, still covered by MoS₂, were compared. It was shown that unlike other widely used methods, the bottom-up approach enabled the atomic-level growth of well-defined MoS₂ slabs on TiO₂ nanostructures, thus aiming to achieve the most effective chemical interactions. In this regard, two kinds of synergistic heterojunctions, namely, crystal face heterojunctions between anatase TiO₂ coexposed {101} and {001} facets and semiconductor heterojunctions between MoS₂ and anatase TiO₂ nanostructures, were considered to play a role in enhancing the photocatalytic activity, together with a proper ratio of (101), (001) coexposed surfaces.

Keywords: shape-tailored TiO₂; 2D MoS₂/TiO₂ heterojunctions; in situ synthesis; photocatalysis



Citation: Santalucia, R.; Negro, P.; Vacca, T.; Pellegrino, F.; Damin, A.; Cesano, F.; Scarano, D. In Situ Assembly of Well-Defined MoS₂ Slabs on Shape-Tailored Anatase TiO₂ Nanostructures: Heterojunctions Role in Phenol Photodegradation. *Catalysts* **2022**, *12*, 1414. <https://doi.org/10.3390/catal12111414>

Academic Editors:

Roberto Comparelli, Ilaria De Pasquale and Chiara Lo Porto

Received: 6 October 2022

Accepted: 7 November 2022

Published: 11 November 2022

Publisher's Note: MDPI stays neutral with regard to jurisdictional claims in published maps and institutional affiliations.



Copyright: © 2022 by the authors. Licensee MDPI, Basel, Switzerland. This article is an open access article distributed under the terms and conditions of the Creative Commons Attribution (CC BY) license (<https://creativecommons.org/licenses/by/4.0/>).

1. Introduction

In recent years, two-dimensional semiconductor heterojunctions have received wide attention due to their novel properties and challenging applications. Among these, many MoS₂/TiO₂-based heterostructures of different dimensionality, made by MoS₂ microflowers, nanotubes, nanobelts, nanosheets, or quantum dots decorating shape-tailored TiO₂ nanoparticles (NPs), have been investigated extensively [1–4]. They are more effective, with respect to the individual MoS₂ and TiO₂-based materials, also for photocatalytic performance and stability in the degradation of pollutants and dyes, renewable and clean energy production, as well electrocatalytic hydrogen production [5], photocatalytic CO₂ reduction [5], applications in solar cells and supercapacitors, up to biomedical fields [6–15].

Concerning the photocatalytic activity, MoS₂/TiO₂-based heterostructures show remarkable properties, including high charge carrier separation and migration efficiencies, together with a wide light harvesting range. Nevertheless, it is well known that TiO₂, albeit an excellent photocatalyst, absorbs only a small portion of the solar spectrum in the UV region (3% of the sunlight spectrum) [7]. Moreover, the photoactivity of anatase TiO₂ suffers significantly from its wide band gap (3.2 eV), high recombination rate of photogenerated electron–hole pairs, and low rate of separation/migration of photoelectrons, for any practical use.

Recently, many efforts have been directed to the modification of TiO₂ in order to obtain photocatalytic activity under visible light, which enables the use of green and renewable-energy-activated processes. Among all the strategies, some approaches consist in the doping/codoping of TiO₂ with heteroelements/metals, or in designing 2D heterostructures alone or coupled with other nanomaterials [16–21] to enhance the photocatalytic activity.

In this concern, due to its absorption in the UV-visible range, together with its high chemical stability, MoS₂ plays a significant role in performing MoS₂/TiO₂ heterojunctions, made by TiO₂ sensitized with MoS₂, thus increasing the visible light absorption ability of TiO₂-based systems [22,23].

However, the stacking characteristics of MoS₂ layered configurations can hinder the active sites on the 2D nanosheets, thus reducing the carrier transfer and, thus, the catalytic activity.

To overcome the limitations of individual materials, the development of MoS₂ nanosheet-hybrid structures provided a way to increase the specific surface area and the dispersion of MoS₂ nanosheets and, thus, the separation time of photoinduced carriers and the photocatalytic activity [24].

Therefore, in order to face the new challenges and opportunities of advanced applications, a deeper understanding of the heterostructure interface in MoS₂/TiO₂-based composites, obtained through careful control of the different crystal growth strategies, must be achieved. For this, the role of the interfaces in affecting the charge transport phenomena or the catalytic processes, which depend on the nature of the dominant faces and, thus, on the arrangement and the atomic structure of the active sites, has been extensively highlighted [25,26]. Concerning this point, model systems of controlled morphology have been designed, including heterostructures of different dimensionality, to achieve a good interfacial contact, thus hindering aggregation phenomena. In particular, two-dimensional layered materials such as transition metal dichalcogenides (TMDs, i.e., MoS₂ and WS₂) have been combined with zero-dimensional (0D) supports, such as plasmonic nanoparticles and quantum dots, or with monodimensional (1D) nanostructures, such as nanotubes, nanowires, and nanoribbons, or also with the two-dimensional ones (2D), to tailor 2D–2D van der Waals hybrid heterostructures [6,13,27–34]. However, to provide a suitable interface contact with supported phases, features such as the surface-to-volume ratio together with the nature of active sites and the extension of the main facets of the support materials have to be considered, as well as the quantum size effects [35–37].

Along this line, highly dispersed MoS₂ nanostructures have been prepared via an in situ bottom-up approach from a suitable molybdenum oxide precursor in a sulfiding atmosphere on many semiconductors, including differently shaped anatase TiO₂ nanostructures [18,38–42]. The bottom-up approach paved the way to the atomic-level growth of well-defined MoS₂ slabs on many TiO₂ nanostructures, including flattened truncated bipyramids or elongated, rod-shaped up to tetragonal cuboids, aiming to achieve the most effective chemical interactions.

Therefore, extensive literature on all these materials concerns a few aspects, including: (i) the possibility to modify and control the ratio of the major TiO₂ facets, (ii) the lattice matching of such TiO₂ surfaces (i.e., {001}, {101}, and {010} facets) with 2D MoS₂ exposed planes to obtain heterojunctions, and (iii) the tuning of the optical properties of heterostructures for enhancing the photocatalytic activity toward visible light. In this context, two kinds of synergistic heterojunctions have been considered, namely, crystal face heterojunctions between anatase TiO₂ coexposed {101} and {001} facets and semiconductor heterojunctions between MoS₂ and anatase TiO₂ nanostructures. According to many authors, it will be shown that a proper ratio of (101), (001) coexposed facets can affect the enhancement of the photocatalytic activity [3,43–45].

However, notwithstanding the great interest in MoS₂/TiO₂ systems, there is a limited number of studies concerning the in situ growth of MoS₂ on different shape-tailored anatase TiO₂ nanostructures.

The aim of this study is to highlight the role played by the morphology and electronic properties of TiO₂-based heterostructures in enabling higher efficiency of photocat-

alysts used in photodegradation processes. In this regard, the relationship between the morphology/structure and vibrational/optical properties of TiO₂ anatase bipyramidal nanoparticles, mainly exposing {101} facets, decorated with MoS₂ slabs, is discussed and the obtained results are compared with the previously published ones on TiO₂ anatase nanosheets exposing both {001} and {101} facets, covered by MoS₂ [6]. In addition, the role of the different facets in affecting the distribution and the dispersion of MoS₂ slabs, together with the investigation of the surface sites on the main exposed faces, is highlighted. It is further confirmed that on samples obtained by the in situ strategy, the MoS₂/surface interaction, that is, the formation of highly dispersed and strongly anchored MoS₂ nanosheets on TiO₂ surfaces, prevents self-aggregation phenomena from occurring. This is shown from FTIR spectra of CO adsorption on MoS₂/TiO₂-combined heterostructures, with the CO molecule being a highly sensitive probe to the nature and the activity of the exposed sites on both nanosheets and bipyramidal TiO₂ anatase nanoparticles. On this matter, it has been reported, from IR spectra of CO adsorbed on pure TiO₂ anatase nanoparticles, that the Lewis acidity and, thus, the activity of Ti⁴⁺ sites on (1 × 4) reconstructed {001} facets of calcined TiO₂ nanosheets are weaker than those of cationic centers on {101} facets of bipyramidal TiO₂ anatase nanoparticles [46].

A comparison between the MoS₂/TiO₂-combined heterostructures in phenol photodegradation highlights the role of the different shapes/facets together with certain features including the surface hydration, the hydroxylation, and the Lewis acidity on the photocatalytic activity.

2. Results and Discussion

2.1. Structure and Morphology of the MoS₂/TiO₂ Nanoparticles by XRD, HRTEM, and Raman Analyses

The crystal structures of MoS₂/TiO₂ n-sh and MoS₂/TiO₂ bipy, obtained via in situ methods, were investigated by X-ray diffraction analysis, and also compared with XRD patterns of MoS₂ bulk (Fluka Chemie AG, Buchs, Switzerland), native TiO₂ n-sh, and TiO₂ bipy powders, used as reference materials. The XRD patterns of the reference materials, already discussed in [46], are summarized and compared with those of MoS₂/TiO₂ n-sh and MoS₂/TiO₂ bipy materials in Figure 1.

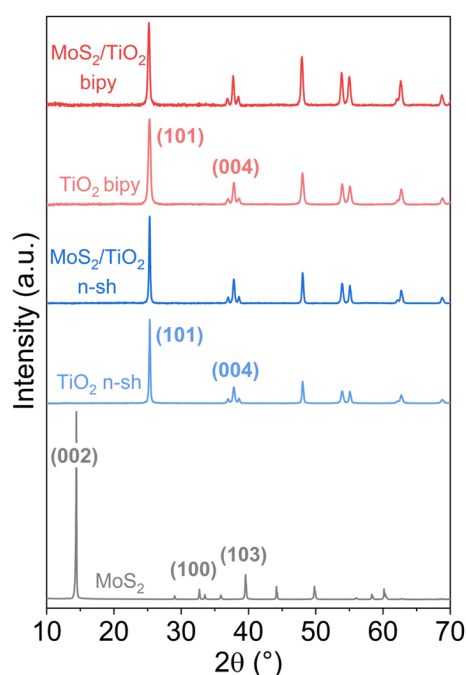


Figure 1. XRD patterns of: MoS₂/TiO₂ bipy (red line), TiO₂ bipy (light red line), MoS₂/TiO₂ n-sh (blue line), TiO₂ n-sh (light blue line), and MoS₂ (grey line).

In this figure, the MoS_2 XRD pattern shows three main peaks at $2\theta = 14.4^\circ$, 32.7° , and at 39.5° , which correspond to the (002), (100), and (103) diffraction planes of hexagonal bulk MoS_2 .

XRD diffraction peaks at $2\theta = 25.2^\circ$, 37.0° , 37.8° , 38.6° , 48.0° , 53.9° , and 55.1° corresponding to (101), (103), (004), (112), (200), (105), and (211) diffraction planes of anatase (PDF card #21-1272) also match well with both the native TiO_2 n-sh and native TiO_2 bipy XRD peaks. Likewise, both in situ-obtained $\text{MoS}_2/\text{TiO}_2$ n-sh and $\text{MoS}_2/\text{TiO}_2$ bipy are quite similar as no MoS_2 XRD diffraction features can be highlighted. By now, it could be hypothesized that, despite a 3 wt.% Mo content, after reaction with H_2S , only a small amount of highly dispersed MoS_2 particles, very small in size (smaller than a few nm), is formed.

The morphology of the differently oriented $\text{MoS}_2/\text{TiO}_2$ n-sh and of $\text{MoS}_2/\text{TiO}_2$ bipy particles is TEM-imaged in Figure 2a,c, with the corresponding analyses of the lateral sizes of the shape-tailored TiO_2 structures, together with the MoS_2 particles stacking order (Figure 2b,d).

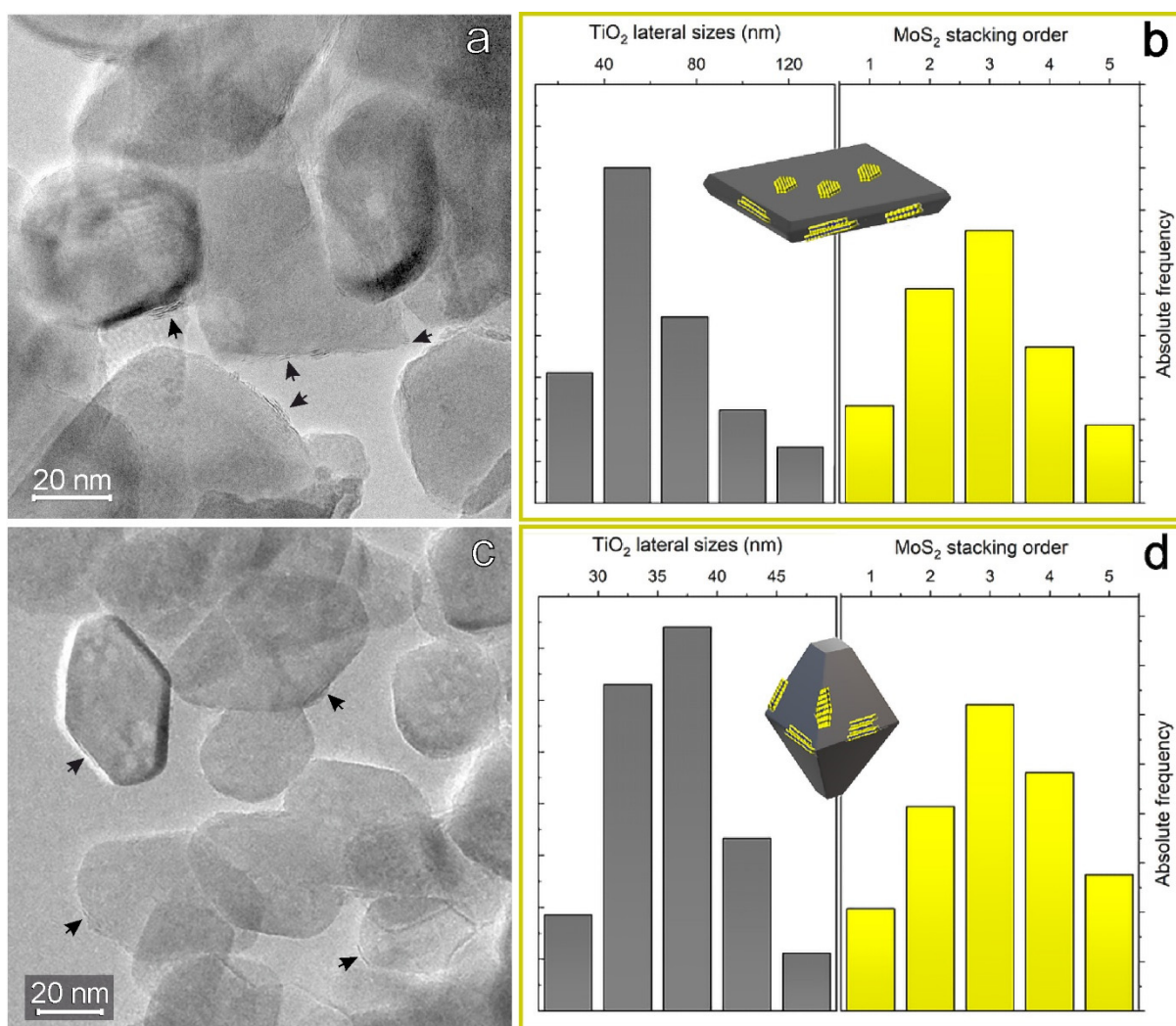


Figure 2. TEM images of: (a) $\text{MoS}_2/\text{TiO}_2$ n-sh and (c) $\text{MoS}_2/\text{TiO}_2$ bipy nanoparticles; lateral size distribution of TiO_2 nanoparticles (grey histograms) and MoS_2 stacking order (yellow histograms) for: (b) $\text{MoS}_2/\text{TiO}_2$ n-sh and (d) $\text{MoS}_2/\text{TiO}_2$ bipy nanoparticles.

Owing to the different orientations with respect to the copper grid, the particles show different contours, due to the random arrangement of the nanocrystals, characterized by prevailing basal (001) faces (Figure 2a) or lateral (101) faces (Figures 2c and S1).

From the TEM image in Figure 2a, $\text{MoS}_2/\text{TiO}_2$ n-sh expose basal faces in the 30–100 nm range, with thicknesses of about 20–30 nm, as obtained from the image contrast.

As far as MoS₂/TiO₂ bipy nanoparticles are concerned, TEM images are shown in Figure 2c. In this figure, truncated bipyramids are 10 nm wide in the basal plane and in the 25–45 nm range along the elongation direction. From particle size analysis, information on the lateral sizes of the TiO₂ n-sh (20–100 nm wide) and TiO₂ bipy (25–45 nm wide) can be obtained at first (gray histograms in Figure 2b,d), in agreement with the TEM images (Figure 2a,c). Some more MoS₂ stacking orders of 3 ± 2 layers come from both systems (yellow histograms in Figure 2b,d), which confirms the effectiveness of the in situ growth in obtaining thinner but even more defective MoS₂ slabs (see later in Figure 3a,b), as compared to other synthesis methods [46]. Despite the low magnification of the TEM images shown in Figure 2a,c, a few curved features decorating the anatase-shaped structures can be noticed (black arrows in figures). Highlighted also in the following HRTEM images (Figure 3a,b), we can ascribe the observed features to interference fringes of MoS₂ layers or dots covering the TiO₂ n-sh and TiO₂ bipy facets.

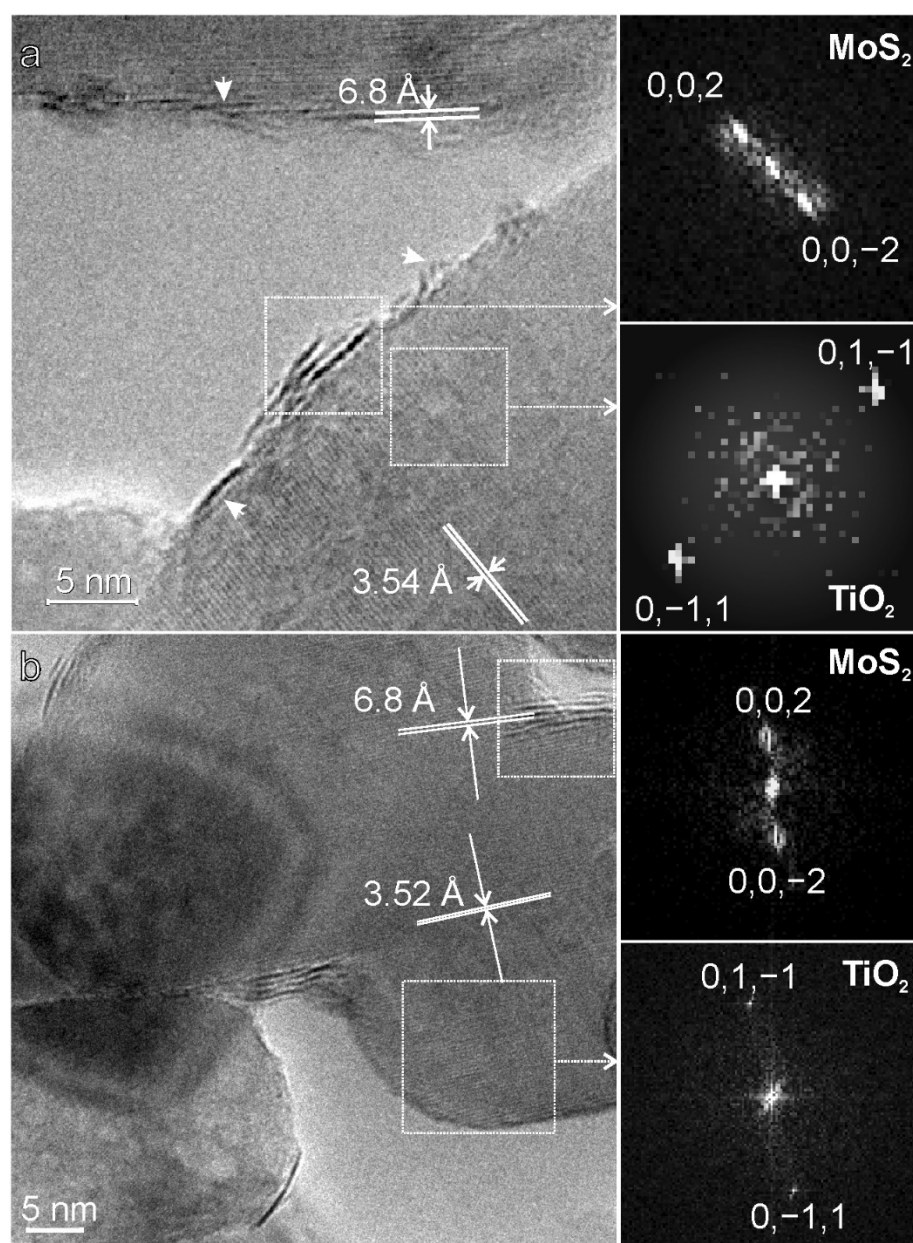


Figure 3. HRTEM images of: (a) MoS₂/TiO₂ n-sh and (b) MoS₂/TiO₂ bipy nanoparticles. In the insets, fast-Fourier-transform (FFT) images of selected regions in a and b are shown.

In particular, from the HRTEM image on a selected region of MoS₂/TiO₂ n-sh nanoparticles (Figure 3a), interference fringes, 3.54 Å apart, that reproduce the crystal planes intersecting the more spaced fringes at the crystal surface are assigned to the (101) planes of anatase. It is expected that the observed interference fringes are parallel to the lateral boundaries of the nanoparticle, confirming that they are the edges between (101) faces, delimiting the more extended basal faces. Interestingly, more irregular fringes, about 6.8 Å spaced, that can be assigned to thin MoS₂, decorate the edges of TiO₂ n-sh, although their presence on basal ones cannot be ruled out [6].

As for MoS₂/TiO₂ bipy, square bidimensional projections of truncated bipyramids with well-defined boundaries are HRTEM-imaged in Figure 3b. The presence of regular interference fringes corresponding to (101) planes of anatase is also observed, together with more irregular fringes, 6.8 Å spaced, assigned to thin MoS₂ slabs, which are anchored either on the extended faces and on the edges.

It is noteworthy that the curved structure of MoS₂ interference fringes, decorating the nanoanatase facets, is indicative of defective situations, including planes and boundaries interruptions, indicating the presence of coordinatively unsaturated atomic sites or reconstruction phenomena [18,22,37,38].

The related fast-Fourier-transform (FFT) images on the right side of Figure 3a,b confirm that the imaged facets correspond to {002} {00-2} {01-1} {0-11} facets on both samples.

Raman spectra of MoS₂/TiO₂ systems, recorded with the 514 nm and 442 nm laser lines, are compared with TiO₂ n-sh, TiO₂ bipy, and MoS₂, used as reference materials, and are shown in Figure 4a,b.

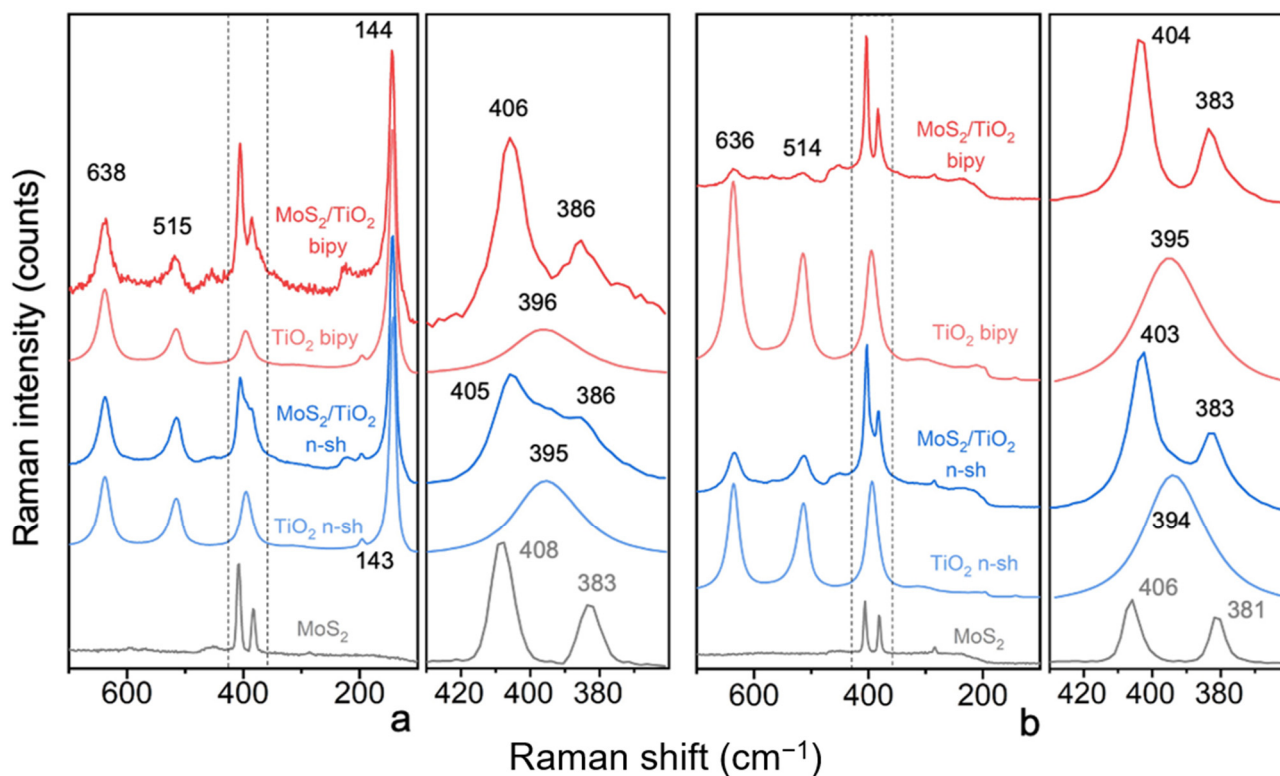


Figure 4. Raman spectra recorded with: (a) $\lambda = 514$ nm and (b) $\lambda = 442$ nm laser lines of: MoS₂/TiO₂ bipy (red line), TiO₂ bipy (light red line), MoS₂/TiO₂ n-sh (blue line), TiO₂ n-sh (light blue line), and bare MoS₂ (grey line) used as a reference material. Enlarged views in the 430–360 cm⁻¹ range have been reported on the right sides of both a and b panels.

Considering, at first, the Raman spectra recorded with the 514 nm laser line, in the 700–100 cm⁻¹ range and in the 430–360 cm⁻¹ enlarged view range, the typical anatase TiO₂ fingerprints can be recognized for both bipyramids and nanosheets structures (Figure 4a).

In this concern, the four bands at 638, 515, 396, and 144 cm^{-1} on TiO_2 bipy and at 638, 515, 395, and 143 cm^{-1} on TiO_2 n-sh are due to the E_g , A_{1g} , B_{1g} , and E_g Raman active modes, respectively, of the anatase phase, as described in the literature [17,47]. It is worth mentioning that the intense E_g Raman mode slightly blueshifts from 143 cm^{-1} to 144 cm^{-1} , moving from anatase nanosheets to bipyramids structures, on more detailed observation. This shift can be explained with phonon confinement effects, due to the decrease in grain size [48].

As for $\text{MoS}_2/\text{TiO}_2$ heterostructures, Raman spectra are compared with those of bare MoS_2 (Figure 4a, enlarged view on the right side). Features centered at 395–396 cm^{-1} observed for $\text{MoS}_2/\text{TiO}_2$ n-sh and $\text{MoS}_2/\text{TiO}_2$ bipy are due to the TiO_2 anatase phase. Such a fingerprint splits into two components at 406 and 386 cm^{-1} (red spectrum, Figure 4a), and at 405 and 386 cm^{-1} (blue spectrum, Figure 4a), which can be ascribed to MoS_2 A_{1g} and E_{12g}^1 first-order Raman active modes, respectively. It is worth noting that in the bulk MoS_2 spectrum, the positions of the A_{1g} and E_{12g}^1 peaks are at 408 and 383 cm^{-1} , respectively.

It is known that the A_{1g} mode is explained with the out-of-plane vibrations of only S atoms in opposite directions, i.e., with a vibration along the stacking of MoS_2 , while the in-plane E_{12g}^1 mode results from the opposite vibration of two S atoms with respect to the Mo atom, and it is related to the lateral extension of the MoS_2 sheets [49]. The asymmetry of both signals is indicative of a variety of sites located on small and differently sized MoS_2 particles. From Figure 4a (enlarged view on the right side), a difference in the frequency values between the A_{1g} and E_{12g}^1 modes of $\cong 20$ cm^{-1} for $\text{MoS}_2/\text{TiO}_2$ bipy, of $\cong 19$ cm^{-1} for $\text{MoS}_2/\text{TiO}_2$ n-sh, and of $\cong 25$ cm^{-1} for the reference bare MoS_2 can be calculated. Based on literature data [38,39,49,50], a relationship between the position of the A_{1g} and E_{12g}^1 vibrational modes and the number of layers in the MoS_2 particles, i.e., indicative of the slab thickness, can be established. Notably, the A_{1g} frequency increases, while the E_{12g}^1 frequency decreases with the thickness, which provides insight into the evolution of the material dimensionality from 2D to 3D structures. Therefore, in order to explain the opposite direction of the frequency shifts, not only van der Waals interlayer coupling, which results in higher force constants and, thus, higher frequency values, but also the presence of long-range Coulombic interlayer interactions together with stacking-induced changes in intralayer bonding are considered [50].

However, by applying the known relationships [49] to $\text{MoS}_2/\text{TiO}_2$ bipy and $\text{MoS}_2/\text{TiO}_2$ n-sh frequency values (Figure 4a), a similar average stacking order of 2 ± 1 layers per particle can be estimated, in agreement with XRD and HRTEM analyses.

It is worth noting that in the case of highly dispersed supported MoS_2 , the particle roughness and curvature together with the growth of peculiar crystal faces and surface defects of the support may affect the shape and positions of the MoS_2 Raman bands, thus meaning that the A_{1g} and E_{12g}^1 mode frequencies cannot provide a clear indication of the MoS_2 stacking order.

Lastly, on both $\text{MoS}_2/\text{TiO}_2$ bipy (red line) and $\text{MoS}_2/\text{TiO}_2$ n-sh (blue line), a small feature at about 200 cm^{-1} can be observed, due to LA phonons at the M point [51]. According to the authors, the intensity ratio between the LA(M) peak and each of the first-order peaks allows to quantify defects in single-layer MoS_2 , which states an analogy between the LA(M) peak in MoS_2 and the D peak in graphene.

Moving to the Raman spectra recorded with the 442 nm laser line, in the 700–100 cm^{-1} range and in the 430–360 cm^{-1} enlarged view range, the typical anatase TiO_2 fingerprints can also be recognized for both bipyramids and nanosheets (light red and light blue lines, respectively), although at lower frequency values due to plausible calibration effects (Figure 4b). However, it is noteworthy that the expected peak at 144–143 cm^{-1} of anatase is absent here, because a filter is used in the experimental setup [39]. From Figure 4b (enlarged view on the right side), a difference in the frequency values between the A_{1g} and E_{12g}^1 modes of $\cong 21$ cm^{-1} for $\text{MoS}_2/\text{TiO}_2$ bipy, of $\cong 20$ cm^{-1} for $\text{MoS}_2/\text{TiO}_2$ n-sh, and of $\cong 25$ cm^{-1} for the reference bare MoS_2 (grey line) can be calculated. However, by applying even the aforementioned relationships [49] to $\text{MoS}_2/\text{TiO}_2$ bipy and $\text{MoS}_2/\text{TiO}_2$ n-sh (Figure 4b), an average stacking order of 2 ± 1 layers per particle can be proved, which is close to that

obtained with the 514 nm laser line and in agreement with XRD and HRTEM analyses too. It is noteworthy that the intensity ratio between TiO_2 and MoS_2 peaks changes, moving from nanosheets to bipyramids particles, thus suggesting a larger amount of MoS_2 domains on the TiO_2 bipy surfaces (vide infra).

2.2. Optical Properties by UV-Vis Spectroscopy

The optical properties of both the sulfided phase and the support, as well as the electronic structure of $\text{MoS}_2/\text{TiO}_2$ bipy and $\text{MoS}_2/\text{TiO}_2$ n-sh, are investigated by comparing their UV-Vis–NIR spectra with those of the TiO_2 bipy, TiO_2 n-sh, and bare MoS_2 (Figure 5).

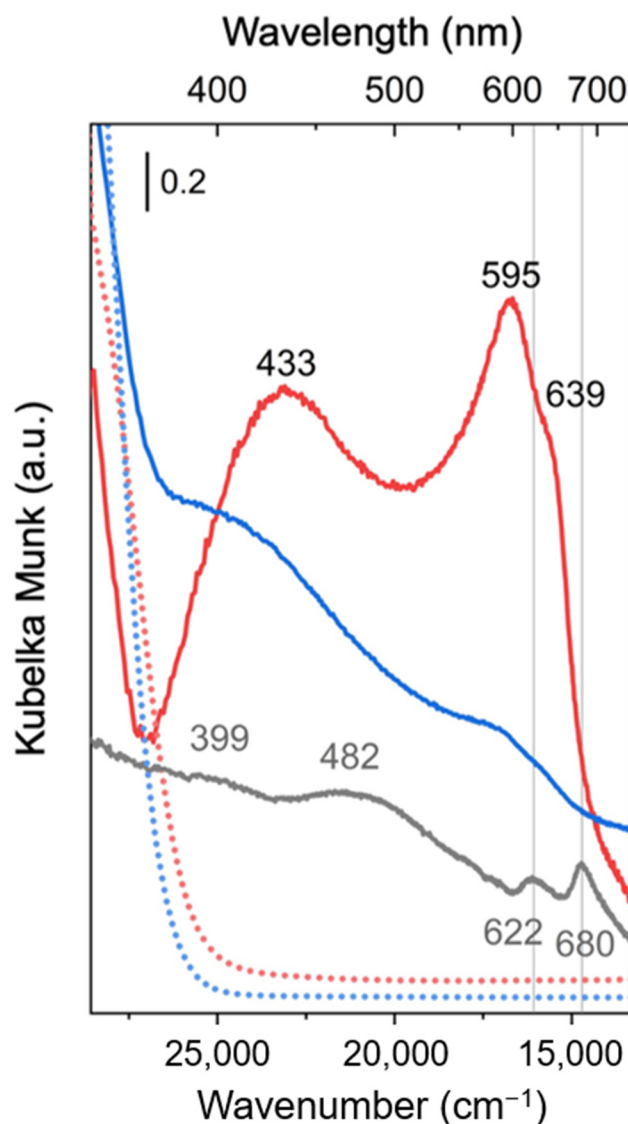


Figure 5. UV-Vis spectra of: $\text{MoS}_2/\text{TiO}_2$ bipy (red line), $\text{MoS}_2/\text{TiO}_2$ n-sh (blue line), TiO_2 bipy (dotted light red line), TiO_2 n-sh (dotted light blue line), and MoS_2 (grey line). For better clarity, the intensities of bulk MoS_2 and of $\text{MoS}_2/\text{TiO}_2$ n-sh spectra are multiplied by a factor of 3 and 2, respectively. The vertical grey dashed lines in the bulk MoS_2 spectrum indicate the position of MoS_2 A and B excitonic transitions. All the spectra are recorded in the diffuse reflectance mode and converted to equivalent absorption Kubelka–Munk units.

UV-Vis spectra of TiO_2 bipy and TiO_2 n-sh show the typical absorption edge of TiO_2 -based systems, due to the transition from the O^{2-} antibonding orbital to the Ti^{4+} lowest-energy orbital [18]. Considering both systems in more detail, a slightly different energy gap

can be observed. In this regard, the TiO₂ n-sh particle thickness is less than that of TiO₂ bipy [46], thus explaining the observed higher bandgap of the nanosheets, which could be due to quantum confinement effects.

According to literature data [52,53] and considering MoS₂ reference spectrum (grey line), the peaks at 680 nm and 622 nm, on the low wavelength side of the 700 nm threshold, are assigned to the A and B direct excitonic transitions, respectively, at the K point of the Brillouin zone [40,41,52,53]. The two excitons are explained with interlayer interactions and spin-orbit splitting effects, that are known to increase with decreasing MoS₂ particle sizes [42]. A second threshold, at about 500 nm, can be assigned also to a direct transition from the deep states in the valence band to the conduction band at the M point of the Brillouin zone. Another excitonic features at 482 nm (C) and 399 nm (D) are also observed on the low wavelength side of this transition [39]. Notice that, although C and D are assigned to direct excitonic transitions at M point, according to some authors [53], it cannot be ruled out the possibility that at least one of them is due to a direct transition at Γ point. Lastly a third threshold at about 350 nm was also ascribed to transitions from deep states in the valence band [40].

From a careful observation of the UV-Vis spectra of MoS₂/TiO₂ bipy and MoS₂/TiO₂ n-sh hybrid systems over the UV-Vis range, at first a wide and continuum absorption, due to the presence of new electronic states, can be highlighted. These are due to the mixing of sulfur 3p atomic orbitals with the TiO₂ valence band, as a consequence of sulfur–oxygen exchange reactions at the surface of TiO₂ nanosheets [17,39]. Concerning the A and B typical excitonic bands for MoS₂/TiO₂ bipy and MoS₂/TiO₂ n-sh hybrid systems, it is noteworthy that they are shifted to higher energies as compared to those of MoS₂ bulk, although to a lesser extent for MoS₂/TiO₂ bipy as compared to the MoS₂/TiO₂ n-sh system.

This behavior is explained in terms of quantum size effects, related to the MoS₂ particle dimensions. In particular, depending on the cluster size, a higher dependence of the frequency shift for C, D excitonic bands has been observed. Therefore, the frequency values of A and B excitons are only slightly blue shifted, whereas remarkable shifts are observed for the C and D excitons [37]. Notice that C and D excitons overlap inside a broad band, as expected for a widely dispersed supported material. These conclusions are in agreement with HRTEM and XRD results

Lastly by comparing MoS₂/TiO₂ bipy and MoS₂/TiO₂ n-sh systems, due to the higher energy of the excitonic transitions in the MoS₂/TiO₂ n-sh system, we can state that the quantum size effects are prevalently concerning with the low dimensionality along c direction, i.e. with the number of layers, although the intra-layer small dimension of MoS₂ platelets can also play a role [54]. By the way, we can conclude that our Raman and UV-visible results are in agreement with the data reported by [46].

2.3. Surface Vibrational Properties by FTIR Spectra of CO Adsorbed on MoS₂/TiO₂ n-sh and on MoS₂/TiO₂ Bipy

FTIR spectra of CO adsorbed at liquid nitrogen temperatures, at decreasing coverages up to the residual pressure of 4×10^{-4} Torr, on the surface of TiO₂ n-sh, pretreated at 873 K, and of MoS₂/TiO₂ n-sh (Mo 3 wt.%) pretreated at 673 K (Figure 6a,b) are compared with those of TiO₂ bipy pretreated at 873 K and of MoS₂/TiO₂ bipy (Mo 3 wt.%) pretreated at 673 K (Figure 7a,b).

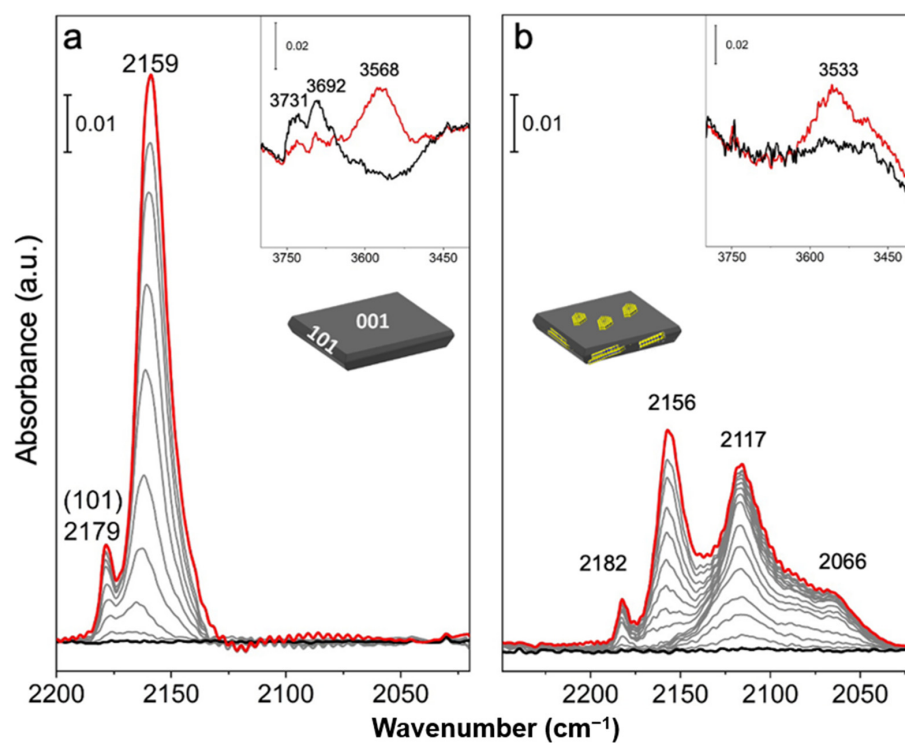


Figure 6. FTIR spectra of CO adsorbed at 77 K (40 Torr, red line) at decreasing coverage up to the residual pressure of 4×10^{-4} Torr (black line) on the surface of: (a) TiO₂ n-sh and (b) MoS₂/TiO₂ n-sh. The insets show the OH vibrational modes regions before (black line) and after CO dosage (red line).

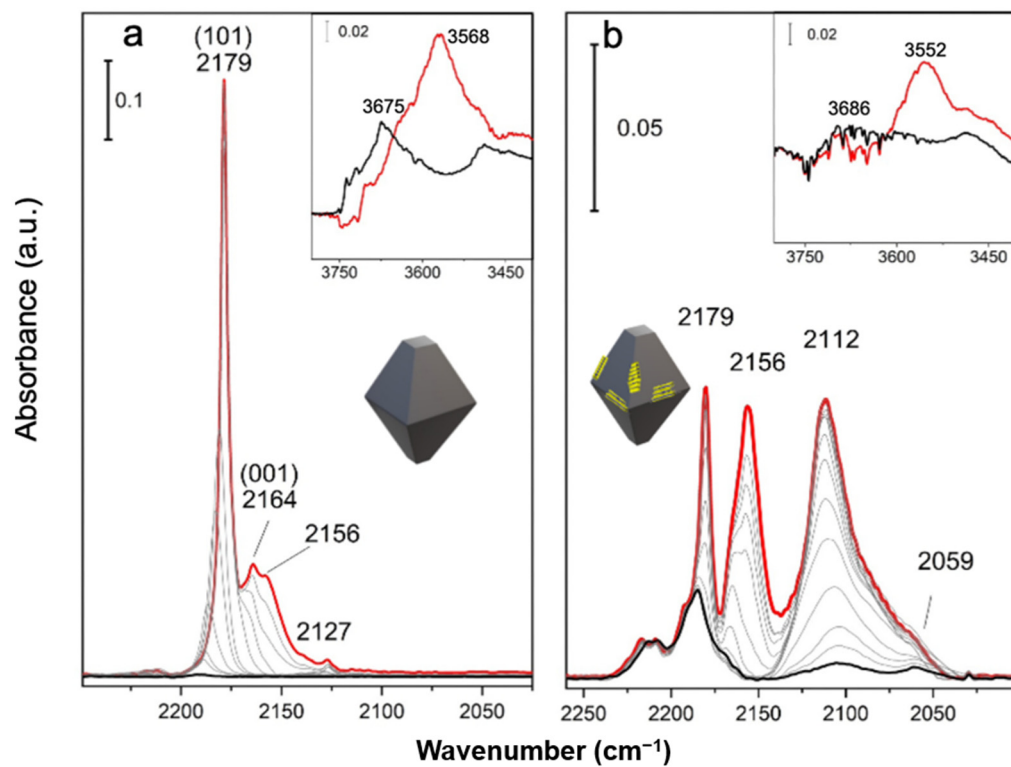


Figure 7. FTIR spectra of CO adsorbed at 77 K (40 Torr, red line) at decreasing coverage up to the residual pressure of 4×10^{-4} Torr (black line) on the surface of: (a) TiO₂ bipy and (b) MoS₂/TiO₂ bipy. The insets show the OH vibrational modes regions before (black line) and after CO dosage (red line).

Therefore, FTIR spectra of CO adsorbed on TiO₂ n-sh and MoS₂/TiO₂ n-sh surfaces [6] can be taken into account, with the aim to compare them with those on TiO₂ bipy and MoS₂/TiO₂ bipy samples.

It is worth noticing that the sulfidation treatment has an influence also on the support matrix (data not reported, for sake of brevity).

The main envelope centered at 2159 cm⁻¹, fully reversible upon CO outgassing (Figure 6a), is due to CO species interacting with the residual surface OH groups on the Ti⁴⁺ sites located on both (1 × 4) reconstructed (001) and (101) surfaces of the TiO₂ n-sh sample, whereas the minor feature observed at 2179 cm⁻¹, almost unaffected by CO outgassing, can be assigned to CO molecules adsorbed on (101) surfaces, less extensive than (001), according to the published data [46]. The complete reversibility of the 2159 cm⁻¹ band is indicative of the weakness of CO interaction on OH groups on Ti⁴⁺ sites [18]. With regard to this, the bands at 3731 and 3692 cm⁻¹, due to the stretching mode of hydroxyl groups present on both the (001) and (101) surfaces, are shifted to lower frequency after CO adsorption, thus giving rise to a broader feature centered at 3568 cm⁻¹ (inset of Figure 6a). The original spectral profile of the hydroxyl groups is fully restored by decreasing the CO gas pressure (spectra not reported for the sake of brevity) together with the progressive disappearance of the 2159 cm⁻¹ band.

As far as the CO spectra on MoS₂/TiO₂ nanosheets (Mo 3 wt.%) are concerned (Figure 6b), at first, a decreased intensity of the adsorption signals on (101) and (001) surfaces is observed, compared to CO spectra on pure TiO₂ n-sh. This fact is explained with a few MoS₂ slabs decorating small surface regions on both {001} and {101} facets, thus causing a lower number of available Ti⁴⁺ and OH sites to interact with CO probe molecules.

In particular, the features at 2179 and 2159 cm⁻¹, already assigned on previous systems to CO molecules adsorbed on Ti⁴⁺ sites on (101) and on OH groups on both (001) and (101) surfaces, respectively, are now observed at 2182 and 2156 cm⁻¹, with a different intensity ratio.

It is worth noting that the asymmetry on the low-frequency side of the band centered at 2156 cm⁻¹ can be explained with CO physisorption on heterogeneous surface sites, including sulfur anions and SH groups, in addition to a few residual OH groups on the (001)/(101) planes of crystalline MoS₂ [55].

In this regard, the wide band observed in the 3600–3400 cm⁻¹ interval (inset of Figure 6b) could be associated with the formation of surface H₂O as a consequence of the oxygen-sulfur exchange and/or of H₂S interaction with surface –OH groups (bonded to Ti⁴⁺) to give rise to hydrogen bonds. Moreover, after CO adsorption, no frequency shift can be observed, thus meaning that OH groups are covered by a few MoS₂ slabs and are, thus, no longer available for any interaction [17,18,39].

However, in the 2130–2050 cm⁻¹ range, two significant features, at 2117 and 2066 cm⁻¹, downshifted with respect to the CO free molecule (2143 cm⁻¹), indicate the formation of surface sites characterized by π-backdonation characteristics (Figure 6b) [56]. In particular, the band at 2117 cm⁻¹ can be ascribed to the Mo^{x+} species (x < 4) located on defective sites (e.g., edges), while the 2066 cm⁻¹ one could be due to the interaction of CO with Mo^{x+} species (x < 4) located on highly coordinatively unsaturated (*cus*) sites such as corners [38]. Such bands are the last to disappear by outgassing and this finding further confirms the presence of isolated and *cus* molybdenum species on defective sites associated with sulfur vacancies, which belong to thin and uniformly distributed MoS₂ slabs, in agreement with Raman and XRD analyses [17].

FTIR spectra of CO adsorbed at 77 K at decreasing coverages up to the residual pressure of 4 × 10⁻⁴ Torr, on the surface of TiO₂ bipy (pretreated at 873 K) and of MoS₂/TiO₂ bipy (Mo 3 wt.%) (pretreated at 673 K), are shown in Figure 7 a,b.

Unlike the CO spectra on TiO₂ n-sh, the main feature of the CO adsorbed on the TiO₂ bipy sample is the band at 2179 cm⁻¹ assigned to the CO molecules adsorbed on Ti⁴⁺ sites on (101) surfaces, which, by decreasing the coverage, shifts reversibly to 2190 cm⁻¹, that is, the frequency of the isolated CO molecule (*ν*CO singleton) (Figure 7a). The full-width at half-height of this band (FWHM = 4 cm⁻¹) is an indication of crystallites delimited by

very large, regular (101) surfaces with no defects. The less intense band at about 2164 cm^{-1} is due to the interaction of CO with Ti^{4+} sites on the less extended (001) surfaces, which also decreases faster than the band at 2179 cm^{-1} as the CO coverage decreases. The high reversibility means a weak interaction on Ti^{4+} sites on (001) surfaces, which behave as even weaker Lewis acid sites. The shoulder around 2156 cm^{-1} indicates the presence of hydrogen interactions between CO and residual OH groups on the surface, located in defective positions (edges, vertices, and steps), as confirmed by the wide band centered at 3675 cm^{-1} , which shifts to 3568 cm^{-1} after CO interaction (inset in Figure 7a) [40]. It is worth noting that the component at 3731 cm^{-1} , before being ascribed to OH groups on highly reactive Ti^{4+} sites of the TiO_2 n-sh (001) surface, is now missing.

The weak signal at 2127 cm^{-1} is finally related to the adsorption of the naturally occurring ^{13}C isotope.

As for the CO spectra on $\text{MoS}_2/\text{TiO}_2$ bipy (Figure 7b), significant changes can be observed. The features at 2179 cm^{-1} and 2156 cm^{-1} , already assigned to CO molecules adsorbed on Ti^{4+} sites on (101) and on residual OH groups, respectively, are also observed, but with a lower intensity and with a different intensity ratio. It is noteworthy that, as the CO coverage decreases, a weak feature on the high-frequency side of the 2156 cm^{-1} band, already assigned to CO interaction with Ti^{4+} sites of the (001) surfaces, appears. In addition, the wide and small band at 3686 cm^{-1} , in the hydroxyl region (inset of Figure 7b), plausibly due to residual OH groups on the main (101) surfaces, shifts to 3552 cm^{-1} as a consequence of CO interaction. The general decrease in intensity can be due to the presence of new Mo^{x+} species, masking the Ti^{4+} sites, which are no longer available for interactions with CO [17,18].

Unlike before, however, the complete desorption of CO from the Ti^{4+} sites on (101) (feature at 2179 cm^{-1}) does not take place, thus indicating a strong energy interaction. In addition, two signals in the $2130\text{--}2050\text{ cm}^{-1}$ range, i.e., at 2112 cm^{-1} and at 2059 cm^{-1} , can be ascribed to reduced Mo^{x+} species ($x < 4$) located on defective sites (e.g., edges).

Lastly, FTIR spectra of CO adsorbed (at 77 K at maximum coverage) on TiO_2 n-sh and $\text{MoS}_2/\text{TiO}_2$ n-sh, and on TiO_2 bipy and $\text{MoS}_2/\text{TiO}_2$ bipy are all compared in Figure 8a,b, respectively.

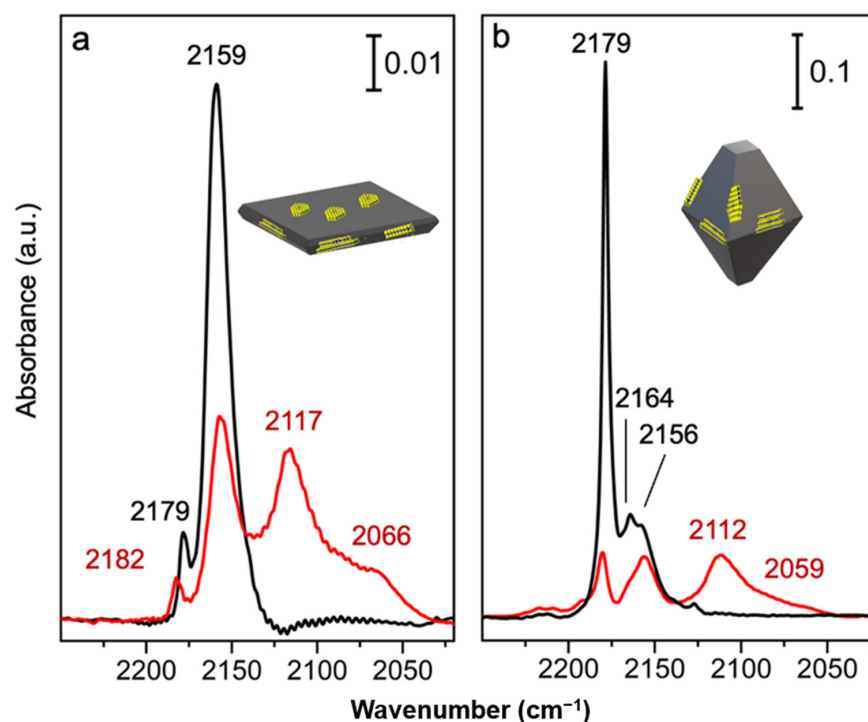


Figure 8. FTIR spectra of CO at 77 K at maximum coverage (40 Torr) adsorbed on the surface of: (a) TiO_2 n-sh (black line) and $\text{MoS}_2/\text{TiO}_2$ n-sh (red line); (b) TiO_2 bipy (black line) and $\text{MoS}_2/\text{TiO}_2$ bipy (red line).

We can conclude that the spectrum of CO on the MoS₂/TiO₂ bipy heterostructure shows a significant intensity decrease of overall signals with respect to CO on TiO₂ bipy, with this behavior even being more remarkable when compared to the CO interaction on MoS₂/TiO₂ n-sh and on TiO₂ n-sh. This could be explained with a larger amount of MoS₂ domains covering the TiO₂ bipy surfaces. According to many authors, despite the lattice mismatch between MoS₂ and TiO₂ [57], the Mo oxysulfide species are responsible for the grafting of MoS₂, either in a parallel or perpendicularly oriented shape at the surface of TiO₂ nanoparticles [39,58]. Density Functional Theory (DFT) calculations, in addition, show a favorable epitaxial relation between the MoS₂ edge sites and (101) anatase surfaces, thus explaining the observed numerous MoS₂ domains on the TiO₂ bipy surfaces [59].

2.4. Photocatalytic Activity

The photocatalytic properties of all the samples are investigated by measuring the decomposition rates of phenol under UV-irradiation ($t = 120$ min, $\lambda_{\max} = 365$ nm) in HClO₄ solution. Results are shown in Figure 9 and Figure S2.

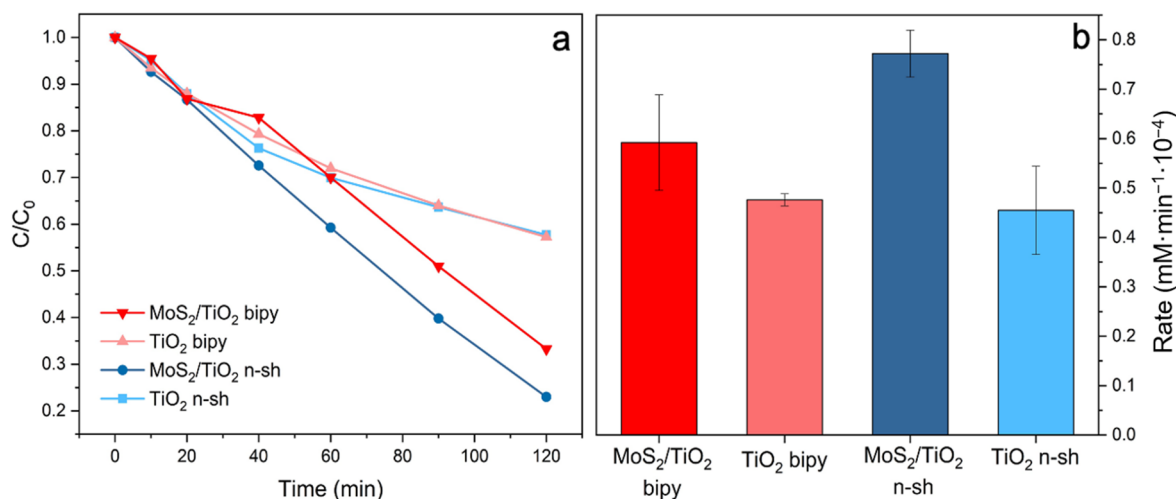


Figure 9. Phenol photocatalytic degradation: (a) relationship between C/C_0 and irradiation time; (b) decomposition rates of: MoS₂/TiO₂ bipy (red curve), TiO₂ bipy (light red curve), MoS₂/TiO₂ n-sh (blue curve), and TiO₂ n-sh (light blue curve).

By comparing the photocatalytic activity of all systems, the fast and continuous decrease in the phenol absorbance intensity can be observed, when phenol mixes with pure and hybrid systems under UV-vis light illumination (Figures 9a and S2).

In Figure 9b, the remarkable role of the MoS₂/TiO₂ heterostructures in the phenol decomposition rate can be highlighted. More in detail, it is inferred that on TiO₂ n-sh and TiO₂ bipy, the photodegradation rate is quite comparable, whereas on MoS₂/TiO₂ n-sh and on MoS₂/TiO₂ bipy heterostructures, a significant enhancement can be evaluated, being more relevant on MoS₂/TiO₂ n-sh heterostructures. The degradation rate of phenol from its initial concentration C_0 could be described by a pseudo-first-order kinetics reaction, in agreement with the Langmuir–Hinshelwood model: $\ln(C_0/C) = kt$, where k is the apparent first-order constant, as obtained in Figure 9b. The obtained degradation rates are in the following order: TiO₂ n-sh \approx TiO₂ bipy < MoS₂/TiO₂ bipy < MoS₂/TiO₂ n-sh, thus confirming the enhanced photoactivity of MoS₂/TiO₂ heterostructures with respect to the pristine TiO₂ systems. Considering the pristine TiO₂ n-sh and TiO₂ bipy, the simultaneous presence of (001) and (101) coexposed surfaces, although with a different ratio (for TiO₂ n-sh: (001)/(101) = 58%/42% and for TiO₂ bipy: (001)/(101) = 13%/87% [46]), is known to give rise to a crystal heterojunction, where photoinduced electrons flow to (101) surfaces, while photoinduced holes flow to (001) surfaces, thus improving the separation efficiency of photoinduced carriers [60]. Hence, despite the higher extension of the more unstable

(001) surfaces on TiO₂ n-sh, together with the slightly lower band gap with respect to TiO₂ bipy, an almost similar photoactivity can be highlighted, with the (001) and (101) surfaces being more effective in phenol oxidation and reduction, respectively.

As for hybrid heterostructures, the photocatalytic activity can be improved. Such an enhancement is due to the presence of MoS₂ nanoparticles, which play a role in reducing charge carrier recombination even more.

More in detail, the MoS₂/TiO₂ bipy heterostructure, because of the prevailing extension of (101) TiO₂ surfaces, could be considered similar to the heterojunction made by P25 with MoS₂, where some carrier recombination effects cannot be ruled out [44]. Conversely, on MoS₂/TiO₂ n-sh, the "double heterojunction" made by combining a crystal heterojunction between (101) and (001) TiO₂ surfaces and a heterojunction between MoS₂ and (001) facets of TiO₂ has a relevant role in affecting the relative position of the conduction and valence bands. As a result of a synergistic effect, the photoinduced holes and electrons produced in TiO₂ can flow into MoS₂ and (101) TiO₂ surfaces, respectively, thus avoiding charge recombination on MoS₂. Based on the aforementioned synergistic effect occurring in the "double heterojunction" between MoS₂ and TiO₂ (101), (001) surfaces on MoS₂/TiO₂ n-sh, we can explain the higher photoactivity toward phenol degradation shown by the MoS₂/TiO₂ n-sh, when compared with the MoS₂/TiO₂ bipy heterostructure.

3. Materials and Methods

3.1. Synthesis of the Samples

The synthesis of both TiO₂ nanostructures is briefly summarized hereafter, because an extensive literature is well known on this theme [6,46,61,62].

3.1.1. TiO₂ Nanosheets

TiO₂ nanosheets were obtained via a solvothermal procedure, that is, 25 mL of Ti(OBu)₄ (titanium (IV) butoxide) was poured in a 150 mL Teflon-lined stainless-steel reactor and 3.5 mL of concentrated hydrofluoric acid was added dropwise under stirring, at 523 K for 24 h. The resulting bluish paste was centrifuged and washed with acetone to remove the residual organics and then with water. Finally, the obtained aqueous suspension was freeze-dried, thus obtaining bluish-powder TiO₂ nanosheets (hereafter TiO₂ n-sh). The subsequent steps are skipped for sake of brevity [6,63–65]. We only remind readers that calcination in air at 873 K, for 60 min, and then cooling down to 298 K in the closed furnace for approximately 10 h were performed to remove the bulk and the surface fluorides.

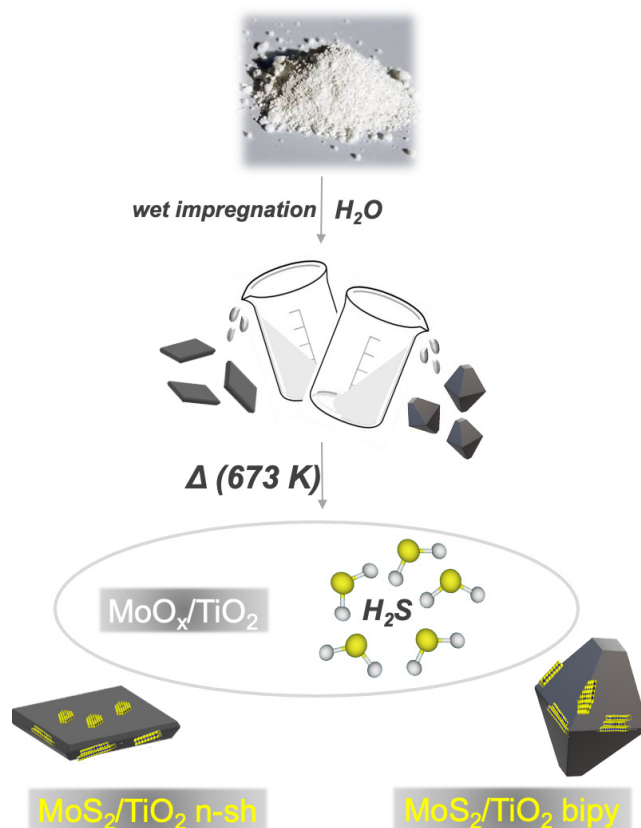
3.1.2. TiO₂ Bipyramidal Nanoparticles

Truncated bipyramidal TiO₂ nanoparticles, hereafter named TiO₂ bipy NPs [46], were obtained by hydrolysis of a 40 mM aqueous solution of Ti (TeoaH)₂ complex (TeoaH = triethanolamine; initial pH 10), carried out by hydrothermal treatment at 493 K for 50 h in an autoclave. The procedure is similar to that developed by Sugimoto but without the intermediate gelation step [66]. Further details on the preparation of TiO₂ bipy NPs, which show a bipyramidal shape, mainly limited by {101} facets, can be found in [62,67].

3.1.3. Synthesis of the MoS₂/TiO₂ n-sh (Nanosheets) and MoS₂/TiO₂ Bipy (Bipyramids) by In Situ Method

The same adopted procedure to obtain MoS₂-decorated TiO₂ nanosheets was carried out also to obtain MoS₂-decorated TiO₂ bipyramids. As already described in our previous paper [6], to which we refer the reader for more details, a distilled water solution of 0.066 g of ammonium heptamolybdate (AHM, (NH₄)₆Mo₇O₂₄·4H₂O) was prepared first. Then, the solution was dripped onto the TiO₂ bipyramids powder (2 g) and mixed with a glass rod. The mixture was placed in an oven at 323 K overnight, to obtain hybrids with Mo 3% by weight. Then, the obtained powder was pressed in a self-supporting pellet by means of a hydraulic press and inserted in a gold frame (suitable for FTIR measurements in situ). Later, the decomposition of AHM into molybdenum oxide (MoO_x) and the removal of

ammonia and water were taken by heat treatment in air at 673 K for 12 h, having set a temperature ramp of 5 K per minute. The MoO_x sample was activated under dynamic vacuum at 673 K for 30 min, and then twice-oxidized in oxygen atmosphere (40 Torr) at the same temperature and time. The oxidized sample was sulfided at 673 K, in the H_2S atmosphere (30 Torr) for 1 h, then outgassed. The sulfidation process was carried out twice. The main steps for both samples are summarized in Scheme 1.



Scheme 1. Main steps of the synthesis process of the $\text{MoS}_2/\text{TiO}_2$ nanosheets and $\text{MoS}_2/\text{TiO}_2$ bipyramids obtained by an in situ method.

3.2. Characterization Methods

The structure and morphology of the samples were investigated by employing the following techniques:

(i) X-ray diffraction (XRD) patterns of samples were collected with a PANalytical PW3050/60 X'Pert PRO MPD diffractometer (Amsterdam, Netherlands) with a Cu anode and a Ni filter, in Bragg–Brentano configuration. The 2θ range was from 10° to 80° with a step size of 0.02° .

(ii) High-resolution transmission electron microscopy (HRTEM) images were obtained with a JEOL 3010-UHR HRTEM microscope (Tokyo, Japan) operating at 300 kV with a point-to-point resolution of 0.12 nm, equipped with a $2\text{ k} \times 2\text{ k}$ pixels Gatan US1000 CCD camera.

(iii) Micro-Raman spectra were acquired in backscattering mode using a Renishaw InVia Raman spectrophotometer (Wotton-Under-Edge, UK), equipped with an Ar+ laser emitting at 514.5 nm ($20\times$ ULWD obj) and an He/Cd laser emitting at 442 nm ($5\times$ obj). The backscattered lights were analyzed by a grid with 1800 lines/mm (for the 514 nm light) and with 2400 lines/nm (for the 442 nm light), then detected by a Peltier cooled CCD detector, with 1 cm^{-1} resolution. The effects of the radiation damage on the samples were reduced by employing 10% of the total laser's emitted power (final power at the sample less than 1 mW) and adopting a homemade setup that allowed the samples to be rotated under the laser beam [68]. This also increased the statistical significance of the measurements [69].

(iv) FTIR spectra were acquired by means of a Bruker IFS 66 FTIR spectrometer (Billerica, MA, USA) equipped with a cryogenic MCT detector with 2 cm^{-1} resolution. Each sample was pressed in the form of a self-supporting pellet with an “optical thickness” of ca. $10\text{ mg}\cdot\text{cm}^{-2}$. To investigate the surface properties, the CO probe molecule was dosed on samples by means of a gas manifold connected to the IR cell, thus allowing us to perform thermal treatments under vacuum and a gas dosage. The spectra were collected after a CO dosage (40 Torr) at 77 K in an IR cell designed for liquid N_2 flow conditions.

(v) The optical properties of the powder samples were studied by means of diffuse reflectance (DR) mode. A Cary 5000 UV-Vis-NIR spectrophotometer (Agilent Technology, Santa Clara, CA, USA), equipped with a diffuse reflectance sphere, was used in the 2500–190 nm wavelength range.

3.3. Photocatalytic Activity

The photocatalytic activities of $\text{MoS}_2/\text{TiO}_2$ n-sh and $\text{MoS}_2/\text{TiO}_2$ bipy, also compared with those of native TiO_2 n-sh and TiO_2 bipy powders, were evaluated by irradiating the suspensions of the samples (loading 100 mg L^{-1} ; pH = 6.5) in cylindrical Pyrex glass cells under magnetic stirring (4 cm diameter, 2.5 cm height, area of $1.26 \times 10^{-3}\text{ m}^2$, cutoff 295 nm, and 5 mL suspension volume), using a fluorescent source with $\lambda_{\text{max}} = 365\text{ nm}$ (Philips PL-S 9W BLB, integrated irradiance = 10 W m^{-2}). Although the phenol absorption on TiO_2 was negligible, before irradiation, the suspension with the substrate was stirred under dark conditions to achieve the equilibrium [70].

Substrate absorption at this wavelength was negligible. The use of this wavelength assured a minimal impact of nanoparticle agglomeration on the photoactivity during the test. The incident radiant power was measured in the range of 290–400 nm with an Ocean Optics USB2000 spectrophotometer (Dunedin, FL, USA), equipped with a cosine-corrected optical fiber probe, spectro-radiometrically calibrated with a NIST traceable DH-2000 CAL UV–vis source (Ocean Optics, Dunedin, FL, USA). The initial nominal concentration of phenol was 0.1 mM. Time profiles of phenol decay were obtained as an average of three irradiation runs. HPLC determination of phenol was carried out with an Agilent Technologies HPLC chromatograph 1200 series (Santa Clara, CA, USA) equipped with a diode array detector, binary gradient high-pressure pump, and an automatic sampler. Isocratic elution was carried out with a mixture of 15/85 acetonitrile/formic acid aqueous solution (0.05% *w/v*), a flow rate of 0.5 mL min^{-1} , and an injection volume of 20 μL . The column used was a Kinetex C18 150-2 (150 mm length, 2 mm i.d., 2.6 μm core–shell particles, Phenomenex, Torrance, CA, USA).

4. Conclusions

Well-defined MoS_2 slabs on shape-tailored anatase TiO_2 structures, i.e., nanosheets and bipyramidal TiO_2 nanoparticles, having a different ratio/extension of (101), (001) coexposed surfaces, are prepared by the in situ method. The peculiar properties of the obtained $\text{MoS}_2/\text{TiO}_2$ heterostructures are investigated to highlight the relevant role played by morphology, structure, stacking order, and defectivity of the MoS_2 slabs toward phenol photodegradation.

More in detail, MoS_2 slabs appear to be thin and defective (i.e., basal plane interruptions, curved structures decorating the anatase facets) with a stacking number of 2 ± 1 layers and basal sizes of 2–10 nm on both systems. The presence of curved MoS_2 slabs decorating the anatase nanosheets and, even more, the bipyramids means that a relevant grafting of MoS_2 particles at the {001} and {101} anatase facets occurs. A further confirmation that MoS_2 slabs are thin and uniformly distributed on the TiO_2 surfaces comes from the presence of new $\text{Mo}^{\text{x+}}$ species on defective sites, masking the Ti^{4+} sites, which are no longer available for interactions with CO.

Furthermore, the sulfidation process affects the reactivity of the support matrix as well, which, in turn, plays a role in the MoS_2 /support interaction.

Concerning the photoactivity properties, on TiO₂ n-sh and TiO₂ bipy, the photodegradation rate is quite comparable, whereas by comparing MoS₂/TiO₂ n-sh and on MoS₂/TiO₂ bipy heterostructures, a significant enhancement on MoS₂/TiO₂ n-sh can be evaluated.

Indeed, on MoS₂/TiO₂ n-sh, the double heterojunction made by combining the crystal heterojunction between (101) and (001) TiO₂ facets and the heterojunction between MoS₂ and TiO₂ (001) facets has a synergistic role in affecting the relative position of the conduction and valence bands, thus causing a higher photoactivity toward phenol degradation of the MoS₂/TiO₂ n-sh with respect to the MoS₂/TiO₂ bipy heterostructure.

Hence, the obtained results can give a contribution to the understanding of the role played by the morphology and optical properties of TiO₂-based heterostructures in enabling a higher efficiency of photocatalysts used in photodegradation processes under UV light irradiation.

In conclusion, we state that hybrid heterostructures can be tailored, by designing suitable preparation methods, also considering the interface structure and then the charge control.

The future prospective of this study can be addressed to visible- and solar-light-driven photocatalytic processes, due to the good photodegradation performances and the optical properties of these nanomaterials, which enable extensive absorption of visible light with the consequent use of green and renewable-energy-activated processes.

Supplementary Materials: The following supporting information can be downloaded at: <https://www.mdpi.com/article/10.3390/catal12111414/s1>, Figure S1: TEM image of MoS₂/bipyramidal TiO₂ nanoparticles with exposed TiO₂ single nanocrystals with the assignment of exposed surfaces; Figure S2: Phenol degradation profiles, expressed as the ratio between concentration after irradiation (C) and concentration before irradiation (C₀) of: (a) MoS₂/TiO₂ bipy (red curve), (b) bipyramidal TiO₂ nanoparticles (light red curve), (c) MoS₂/TiO₂ n-sh (blue curve), and (d) TiO₂ nanosheets.

Author Contributions: F.C., A.D., P.N., F.P., R.S., D.S. and T.V. wrote and organized the manuscript; F.C., A.D., P.N., F.P., R.S. and T.V. performed experiments and characterizations. In particular, F.C. performed XRD and TEM analyses; A.D. performed Raman analyses; F.P. contributed to sample preparation and photocatalytic analysis; P.N., R.S. and T.V. performed FTIR and UV-Vis analyses; D.S., F.C., P.N. and R.S. provided a substantial contribution to the work; D.S. supervised the manuscript. All authors have read and agreed to the published version of the manuscript.

Funding: This research received no external funding.

Data Availability Statement: The data presented in this study are available on request from the corresponding author.

Acknowledgments: This work was supported by MUR (Ministero dell'Università e della Ricerca), INSTM Consorzio, and NIS (Nanostructured Interfaces and Surfaces) Inter-Departmental Center of University of Torino. The authors thank the Laboratory of the Chemistry Department and, in particular, Valsania, M.C., and Maurino, V.

Conflicts of Interest: The authors declare no conflict of interest.

References

1. Yang, X.; Huang, H.; Jin, B.; Luo, J.; Zhou, X. Facile synthesis of MoS₂/B-TiO₂ nanosheets with exposed {001} facets and enhanced visible-light-driven photocatalytic H₂ production activity. *RSC Adv.* **2016**, *6*, 107075–107080. [CrossRef]
2. Chen, C.; Xin, X.; Zhang, J.; Li, G.; Zhang, Y.; Lu, H.; Gao, J.; Yang, Z.; Wang, C.; He, Z. Few-Layered MoS₂ Nanoparticles Loaded TiO₂ Nanosheets with Exposed {001} Facets for Enhanced Photocatalytic Activity. *Nano* **2018**, *13*, 1850129. [CrossRef]
3. Zhang, J.; Huang, L.; Lu, Z.; Jin, Z.; Wang, X.; Xu, G.; Zhang, E.; Wang, H.; Kong, Z.; Xi, J.; et al. Crystal face regulating MoS₂/TiO₂ (001) heterostructure for high photocatalytic activity. *J. Alloys Compd.* **2016**, *688*, 840–848. [CrossRef]
4. Cao, L.; Wang, R.; Wang, D.; Li, X.; Jia, H. MoS₂-hybridized TiO₂ nanosheets with exposed {001} facets to enhance the visible-light photocatalytic activity. *Mater. Lett.* **2015**, *160*, 286–290. [CrossRef]
5. Jia, P.-Y.; Guo, R.-T.; Pan, W.-G.; Huang, C.-Y.; Tang, J.-Y.; Liu, X.-Y.; Qin, H.; Xu, Q.-Y. The MoS₂/TiO₂ heterojunction composites with enhanced activity for CO₂ photocatalytic reduction under visible light irradiation. *Coll. Surf. A Phys. Engin. Asp.* **2019**, *570*, 306–316. [CrossRef]
6. Santalucia, R.; Vacca, T.; Cesano, F.; Martra, G.; Pellegrino, F.; Scarano, D. Few-layered MoS₂ nanoparticles covering anatase TiO₂ nanosheets: Comparison between ex situ and in situ synthesis approaches. *Appl. Sci.* **2021**, *11*, 143. [CrossRef]

7. Chatterjee, D.; Mahata, A. Visible light induced photodegradation of organic pollutants on dye adsorbed TiO₂ surface. *J. Photochem. Photob. A Chem.* **2002**, *153*, 199–204. [[CrossRef](#)]
8. Matos, J.; García, A.; Zhao, L.; Titirici, M.M. Solvothermal carbon-doped TiO₂ photocatalyst for the enhanced methylene blue degradation under visible light. *Appl. Catal. A Gen.* **2010**, *390*, 175–182. [[CrossRef](#)]
9. Cheng, Y.; Geng, H.; Huang, X. Advanced water splitting electrocatalysts via the design of multicomponent heterostructures. *Dalton Trans.* **2020**, *49*, 2761–2765. [[CrossRef](#)]
10. Uddin, M.J.; Daramola, D.; Velasquez, E.; Dickens, T.; Yan, J.; Hammel, E.; Cesano, F.; Okoli, O.I. A high efficiency 3D photovoltaic microwire with carbon nanotubes (CNT)-quantum dot (QD) hybrid interface. *Phys. Status Solidi (RRL)—Rapid Res. Lett.* **2014**, *8*, 898–903. [[CrossRef](#)]
11. Wang, H.; Liu, F.; Fu, W.; Fang, Z.; Zhou, W.; Liu, Z. Two-dimensional heterostructures: Fabrication, characterization, and application. *Nanoscale* **2014**, *6*, 12250–12272. [[CrossRef](#)] [[PubMed](#)]
12. Wang, Z.; Mi, B. Environmental Applications of 2D Molybdenum Disulfide (MoS₂) Nanosheets. *Environ. Sci. Technol.* **2017**, *51*, 8229–8244. [[CrossRef](#)] [[PubMed](#)]
13. Yuan, Y.-J.; Ye, Z.-J.; Lu, H.-W.; Hu, B.; Li, Y.-H.; Chen, D.-Q.; Zhong, J.-S.; Yu, Z.-T.; Zou, Z.-G. Constructing Anatase TiO₂ Nanosheets with Exposed (001) Facets/Layered MoS₂ Two-Dimensional Nanojunctions for Enhanced Solar Hydrogen Generation. *ACS Catal.* **2016**, *6*, 532–541. [[CrossRef](#)]
14. Chen, B.; Meng, Y.; Sha, J.; Zhong, C.; Hu, W.; Zhao, N. Preparation of MoS₂/TiO₂ based nanocomposites for photocatalysis and rechargeable batteries: Progress, challenges, and perspective. *Nanoscale* **2018**, *10*, 34–68. [[CrossRef](#)] [[PubMed](#)]
15. Cesano, F.; Pellerej, D.; Scarano, D.; Ricchiardi, G.; Zecchina, A. Radially organized pillars of TiO₂ nanoparticles: Synthesis, characterization and photocatalytic tests. *J. Photochem. Photob. A Chem.* **2012**, *242*, 51–58. [[CrossRef](#)]
16. Haque, M.M.; Khan, A.; Umar, K.; Mir, N.A.; Muneer, M.; Harada, T.; Matsumura, M. Synthesis, Characterization and Photocatalytic Activity of Visible Light Induced Ni-Doped TiO₂. *Energy Environ. Focus* **2013**, *2*, 73–78. [[CrossRef](#)]
17. Cravanzola, S.; Cesano, F.; Gaziano, F.; Scarano, D. Sulfur-Doped TiO₂: Structure and Surface Properties. *Catalysts* **2017**, *7*, 214. [[CrossRef](#)]
18. Scarano, D.; Cesano, F.; Zecchina, A. MoS₂ Domains on TiO₂-Based Nanostructures: Role of Titanate/TiO₂ Transformation and Sulfur Doping on the Interaction with the Support. *J. Phys. Chem. C* **2019**, *123*, 7799–7809. [[CrossRef](#)]
19. Yashwanth, H.J.; Rondiya, S.R.; Dzade, N.Y.; Hoye, R.L.Z.; Choudhary, R.J.; Phase, D.M.; Dhole, S.D.; Hareesh, K. Improved photocatalytic activity of TiO₂ nanoparticles through nitrogen and phosphorus co-doped carbon quantum dots: An experimental and theoretical study. *Phys. Chem. Chem. Phys.* **2022**, *24*, 15271–15279. [[CrossRef](#)]
20. Wang, Y.; Ding, Z.; Arif, N.; Jiang, W.-C.; Zeng, Y.-J. 2D material based heterostructures for solar light driven photocatalytic H₂ production. *Mater. Adv.* **2022**, *3*, 3389–3417. [[CrossRef](#)]
21. Du, R.; Li, B.; Han, X.; Xiao, K.; Wang, X.; Zhang, C.; Arbiol, J.; Cabot, A. 2D/2D Heterojunction of TiO₂ Nanoparticles and Ultrathin g-C₃N₄ Nanosheets for Efficient Photocatalytic Hydrogen Evolution. *Nanomaterials* **2022**, *12*, 1557. [[CrossRef](#)] [[PubMed](#)]
22. Cravanzola, S.; Sarro, M.; Cesano, F.; Calza, P.; Scarano, D. Few-Layer MoS₂ Nanodomains Decorating TiO₂ Nanoparticles: A Case Study for the Photodegradation of Carbamazepine. *Nanomaterials* **2018**, *8*, 207. [[CrossRef](#)] [[PubMed](#)]
23. Kumar, S.G.; Devi, L.G. Review on Modified TiO₂ Photocatalysis under UV/Visible Light: Selected Results and Related Mechanisms on Interfacial Charge Carrier Transfer Dynamics. *J. Phys. Chem. A* **2011**, *115*, 13211–13241. [[CrossRef](#)] [[PubMed](#)]
24. Shen, M.; Yan, Z.; Yang, L.; Du, P.; Zhang, J.; Xiang, B. MoS₂ nanosheet/TiO₂ nanowire hybrid nanostructures for enhanced visible-light photocatalytic activities. *Chem. Commun.* **2014**, *50*, 15447–15449. [[CrossRef](#)] [[PubMed](#)]
25. Schneider, W.-D.; Heyde, M.; Freund, H.-J. Charge Control in Model Catalysis: The Decisive Role of the Oxide–Nanoparticle Interface. *Chem. A Eur. J.* **2018**, *24*, 2317–2327. [[CrossRef](#)] [[PubMed](#)]
26. Hu, K.H.; Hu, X.G.; Xu, Y.F.; Pan, X.Z. The effect of morphology and size on the photocatalytic properties of MoS₂. *React. Kinet. Mech. Catal.* **2010**, *100*, 153–163. [[CrossRef](#)]
27. Goswami, N.; Giri, A.; Pal, S.K. MoS₂ Nanocrystals Confined in a DNA Matrix Exhibiting Energy Transfer. *Langmuir* **2013**, *29*, 11471–11478. [[CrossRef](#)]
28. Lee, Y.-H.; Zhang, X.-Q.; Zhang, W.; Chang, M.-T.; Lin, C.-T.; Chang, K.-D.; Yu, Y.-C.; Wang, J.T.-W.; Chang, C.-S.; Li, L.-J.; et al. Synthesis of large-area MoS₂ atomic layers with chemical vapor deposition. *Adv. Mater.* **2012**, *24*, 2320–2325. [[CrossRef](#)]
29. Stephenson, T.; Li, Z.; Olsen, B.; Mitlin, D. Lithium ion battery applications of molybdenum disulfide (MoS₂) nanocomposites. *Energy Environ. Sci.* **2014**, *7*, 209–231. [[CrossRef](#)]
30. Lin, Y.; Ren, P.; Wei, C. Fabrication of MoS₂/TiO₂ heterostructures with enhanced photocatalytic activity. *CrystEngComm* **2019**, *21*, 3439–3450. [[CrossRef](#)]
31. Wan, J.; Lacey, S.D.; Dai, J.; Bao, W.; Fuhrer, M.S.; Hu, L. Tuning two-dimensional nanomaterials by intercalation: Materials, properties and applications. *Chem. Soc. Rev.* **2016**, *45*, 6742–6765. [[CrossRef](#)] [[PubMed](#)]
32. Sreepal, V.; Yagmurcukardes, M.; Vasu, K.S.; Kelly, D.J.; Taylor, S.F.R.; Kravets, V.G.; Kudrynskyi, Z.; Kovalyuk, Z.D.; Patanè, A.; Grigorenko, A.N.; et al. Two-Dimensional Covalent Crystals by Chemical Conversion of Thin van der Waals Materials. *Nano Lett.* **2019**, *19*, 6475–6481. [[CrossRef](#)] [[PubMed](#)]
33. Zhao, X.; Song, P.; Wang, C.; Riis-Jensen, A.C.; Fu, W.; Deng, Y.; Wan, D.; Kang, L.; Ning, S.; Dan, J.; et al. Engineering covalently bonded 2D layered materials by self-intercalation. *Nature* **2020**, *581*, 171–177. [[CrossRef](#)]
34. Geim, A.K.; Grigorieva, I.V. Van der Waals heterostructures. *Nature* **2013**, *499*, 419–425. [[CrossRef](#)] [[PubMed](#)]

35. Mao, Y.; Wong, S.S. Size- and Shape-Dependent Transformation of Nanosized Titanate into Analogous Anatase Titania Nanostructures. *JACS* **2006**, *128*, 8217–8226. [[CrossRef](#)] [[PubMed](#)]
36. Kitano, M.; Wada, E.; Nakajima, K.; Hayashi, S.; Miyazaki, S.; Kobayashi, H.; Hara, M. Protonated Titanate Nanotubes with Lewis and Brønsted Acidity: Relationship between Nanotube Structure and Catalytic Activity. *Chem. Mater.* **2013**, *25*, 385–393. [[CrossRef](#)]
37. Cravanzola, S.; Muscuso, L.; Cesano, F.; Agostini, G.; Damin, A.; Scarano, D.; Zecchina, A. MoS₂ Nanoparticles Decorating Titanate-Nanotube Surfaces: Combined Microscopy, Spectroscopy, and Catalytic Studies. *Langmuir* **2015**, *31*, 5469–5478. [[CrossRef](#)]
38. Cesano, F.; Bertarione, S.; Piovano, A.; Agostini, G.; Rahman, M.M.; Groppo, E.; Bonino, F.; Scarano, D.; Lamberti, C.; Bordiga, S.; et al. Model oxide supported MoS₂ HDS catalysts: Structure and surface properties. *Catal. Sci. Technol.* **2011**, *1*, 123–136. [[CrossRef](#)]
39. Cravanzola, S.; Cesano, F.; Gaziano, F.; Scarano, D. Carbon Domains on MoS₂/TiO₂ System via Catalytic Acetylene Oligomerization: Synthesis, Structure, and Surface Properties. *Front. Chem.* **2017**, *5*, 91. [[CrossRef](#)]
40. Cesano, F.; Bertarione, S.; Uddin, M.J.; Agostini, G.; Scarano, D.; Zecchina, A. Designing TiO₂ Based Nanostructures by Control of Surface Morphology of Pure and Silver Loaded Titanate Nanotubes. *J. Phys. Chem. C* **2010**, *114*, 169–178. [[CrossRef](#)]
41. Bavykin, D.V.; Friedrich, J.M.; Walsh, F.C. Protonated Titanates and TiO₂ Nanostructured Materials: Synthesis, Properties, and Applications. *Adv. Mater.* **2006**, *18*, 2807–2824. [[CrossRef](#)]
42. Cesano, F.; Cravanzola, S.; Rahman, M.M.; Scarano, D. Interplay between Fe-Titanate Nanotube Fragmentation and Catalytic Decomposition of C₂H₄: Formation of C/TiO₂ Hybrid Interfaces. *Inorganics* **2018**, *6*, 55. [[CrossRef](#)]
43. Pan, J.; Liu, G.; Lu, G.Q.M.; Cheng, H.-M. On the True Photoreactivity Order of {001}, {010}, and {101} Facets of Anatase TiO₂ Crystals. *Angew. Chem. Int. Ed.* **2011**, *50*, 2133–2137. [[CrossRef](#)] [[PubMed](#)]
44. Zhang, J.; Zhang, L.; Yu, W.; Jiang, F.; Zhang, E.; Wang, H.; Kong, Z.; Xi, J.; Ji, Z. Novel dual heterojunction between MoS₂ and anatase TiO₂ with coexposed {101} and {001} facets. *J. Am. Ceram. Soc.* **2017**, *100*, 5274–5285. [[CrossRef](#)]
45. Zhang, J.; Zhang, L.; Ma, X.; Ji, Z. A study of constructing heterojunction between two-dimensional transition metal sulfides (MoS₂ and WS₂) and (101), (001) faces of TiO₂. *Appl. Surf. Sci.* **2018**, *430*, 424–437. [[CrossRef](#)]
46. Mino, L.; Pellegrino, F.; Rades, S.; Radnik, J.; Hodoroaba, V.-D.; Spoto, G.; Maurino, V.; Martra, G. Beyond Shape Engineering of TiO₂ Nanoparticles: Post-Synthesis Treatment Dependence of Surface Hydration, Hydroxylation, Lewis Acidity and Photocatalytic Activity of TiO₂ Anatase Nanoparticles with Dominant {001} or {101} Facets. *ACS Appl. Nano Mater.* **2018**, *1*, 5355–5365. [[CrossRef](#)]
47. Kumar, S.; Shakya, J.; Mohanty, T. Probing interfacial charge transfer dynamics in MoS₂/TiO₂ nanocomposites using scanning Kelvin probe for improved photocatalytic response. *Surf. Sci.* **2020**, *693*, 121530. [[CrossRef](#)]
48. Zhu, K.-R.; Zhang, M.-S.; Chen, Q.; Yin, Z. Size and phonon-confinement effects on low-frequency Raman mode of anatase TiO₂ nanocrystal. *Phys. Lett. A* **2005**, *340*, 220–227. [[CrossRef](#)]
49. Li, H.; Zhang, Q.; Yap, C.C.R.; Tay, B.K.; Edwin, T.H.T.; Olivier, A.; Baillargeat, D. From Bulk to Monolayer MoS₂: Evolution of Raman Scattering. *Adv. Funct. Mater.* **2012**, *22*, 1385–1390. [[CrossRef](#)]
50. Lee, C.; Yan, H.; Brus, L.E.; Heinz, T.F.; Hone, J.; Ryu, S. Anomalous Lattice Vibrations of Single- and Few-Layer MoS₂. *ACS Nano* **2010**, *4*, 2695–2700. [[CrossRef](#)]
51. Mignuzzi, S.; Pollard, A.J.; Bonini, N.; Brennan, B.; Gilmore, I.S.; Pimenta, M.A.; Richards, D.; Roy, D. Effect of disorder on Raman scattering of single-layer MoS₂. *Phys. Rev. B Condens. Matter Mater. Phys.* **2015**, *91*, 195411. [[CrossRef](#)]
52. Muscuso, L.; Cravanzola, S.; Cesano, F.; Scarano, D.; Zecchina, A. Optical, Vibrational, and Structural Properties of MoS₂ Nanoparticles Obtained by Exfoliation and Fragmentation via Ultrasound Cavitation in Isopropyl Alcohol. *J. Phys. Chem. C* **2015**, *119*, 3791–3801. [[CrossRef](#)]
53. Wilcoxon, J.P.; Newcomer, P.P.; Samara, G.A. Synthesis and optical properties of MoS₂ and isomorphous nanoclusters in the quantum confinement regime. *J. Appl. Phys.* **1997**, *81*, 7934–7944. [[CrossRef](#)]
54. Shi, H.; Yan, R.; Bertolazzi, S.; Brivio, J.; Gao, B.; Kis, A.; Jena, D.; Xing, H.G.; Huang, L. Exciton Dynamics in Suspended Monolayer and Few-Layer MoS₂ 2D Crystals. *ACS Nano* **2013**, *7*, 1072–1080. [[CrossRef](#)] [[PubMed](#)]
55. Tsyganenko, A.A.; Can, F.; Travert, A.; Maugé, F. FTIR study of unsupported molybdenum sulfide—In situ synthesis and surface properties characterization. *Appl. Catal. A Gen.* **2004**, *268*, 189–197. [[CrossRef](#)]
56. Bolis, V.; Barbaglia, A.; Bordiga, S.; Lamberti, C.; Zecchina, A. Heterogeneous Nonclassical Carbonyls Stabilized in Cu(I)- and Ag(I)-ZSM-5 Zeolites: Thermodynamic and Spectroscopic Features. *J. Phys. Chem. B* **2004**, *108*, 9970–9983. [[CrossRef](#)]
57. Dai, R.; Zhang, A.; Pan, Z.; Al-Enizi, A.M.; Elzatahry, A.A.; Hu, L.; Zheng, G. Epitaxial Growth of Lattice-Mismatched Core-Shell TiO₂@MoS₂ for Enhanced Lithium-Ion Storage. *Small* **2016**, *12*, 2792–2799. [[CrossRef](#)]
58. Kibsgaard, J.; Clausen, B.S.; Topsøe, H.; Lægsgaard, E.; Lauritsen, J.V.; Besenbacher, F. Scanning tunneling microscopy studies of TiO₂-supported hydrotreating catalysts: Anisotropic particle shapes by edge-specific MoS₂-support bonding. *J. Catal.* **2009**, *263*, 98–103. [[CrossRef](#)]
59. Arrouvel, C.; Breyse, M.; Toulhoat, H.; Raybaud, P. A density functional theory comparison of anatase (TiO₂)- and γ -Al₂O₃-supported MoS₂ catalysts. *J. Catal.* **2005**, *232*, 161–178. [[CrossRef](#)]
60. Yu, J.; Low, J.; Xiao, W.; Zhou, P.; Jaroniec, M. Enhanced Photocatalytic CO₂-Reduction Activity of Anatase TiO₂ by Coexposed {001} and {101} Facets. *JACS* **2014**, *136*, 8839–8842. [[CrossRef](#)]
61. Zhang, Y.; Cai, J.; Ma, Y.; Qi, L. Mesocrystalline TiO₂ nanosheet arrays with exposed {001} facets: Synthesis via topotactic transformation and applications in dye-sensitized solar cells. *Nano Res.* **2017**, *10*, 2610–2625. [[CrossRef](#)]

62. Deiana, C.; Minella, M.; Tabacchi, G.; Maurino, V.; Fois, E.; Martra, G. Shape-controlled TiO₂ nanoparticles and TiO₂ P25 interacting with CO and H₂O₂ molecular probes: A synergic approach for surface structure recognition and physico-chemical understanding. *Phys. Chem. Chem. Phys.* **2013**, *15*, 307–315. [[CrossRef](#)] [[PubMed](#)]
63. Panayotov, D.A.; Burrows, S.P.; Morris, J.R. Infrared Spectroscopic Studies of Conduction Band and Trapped Electrons in UV-Photoexcited, H-Atom n-Doped, and Thermally Reduced TiO₂. *J. Phys. Chem. C* **2012**, *116*, 4535–4544. [[CrossRef](#)]
64. Jangir, M.; Jain, A.; Yamaguchi, S.; Ichikawa, T.; Lal, C.; Jain, I.P. Catalytic effect of TiF₄ in improving hydrogen storage properties of MgH₂. *Int. J. Hydrogen Energy* **2016**, *41*, 14178–14183. [[CrossRef](#)]
65. Radnik, J.; Mohr, C.; Claus, P. On the origin of binding energy shifts of core levels of supported gold nanoparticles and dependence of pretreatment and material synthesis. *Phys. Chem. Chem. Phys.* **2003**, *5*, 172–177. [[CrossRef](#)]
66. Sugimoto, T.; Zhou, X.; Muramatsu, A. Synthesis of uniform anatase TiO₂ nanoparticles by gel–sol method: 3. Formation process and size control. *J. Colloid Interface Sci.* **2003**, *259*, 43–52. [[CrossRef](#)]
67. Pellegrino, F.; Isopescu, R.; Pellutiè, L.; Sordello, F.; Rossi, A.M.; Ortel, E.; Martra, G.; Hodoroaba, V.D.; Maurino, V. Machine learning approach for elucidating and predicting the role of synthesis parameters on the shape and size of TiO₂ nanoparticles. *Sci. Rep.* **2020**, *10*, 18910. [[CrossRef](#)]
68. Signorile, M.; Bonino, F.; Damin, A.; Bordiga, S. A Novel Raman Setup Based on Magnetic-Driven Rotation of Sample. *Top. Catal.* **2018**, *61*, 1491–1498. [[CrossRef](#)]
69. Menzyk, A.; Damin, A.; Martyna, A.; Alladio, E.; Vincenti, M.; Martra, G.; Zadora, G. Toward a novel framework for bloodstains dating by Raman spectroscopy: How to avoid sample photodamage and subsampling errors. *Talanta* **2020**, *209*, 120565. [[CrossRef](#)]
70. Pellegrino, F.; Pellutiè, L.; Sordello, F.; Minero, C.; Ortel, E.; Hodoroaba, V.-D.; Maurino, V. Influence of agglomeration and aggregation on the photocatalytic activity of TiO₂ nanoparticles. *Appl. Catal. B Environm.* **2017**, *216*, 80–87. [[CrossRef](#)]